

Ultrafast electron dynamics in Au/Fe/MgO(001) analyzed by Au- and Fe-selective pumping in time-resolved two-photon photoemission spectroscopy: Separation of excitations in adjacent metallic layers

Y. Beyazit,¹ F. Kühne,¹ D. Diesing,² P. Zhou,¹ J. Jayabalan ,¹ B. Sothmann ,¹ and U. Bovensiepen ,^{1,3,*}

¹*Faculty of Physics and Center for Nanointegration (CENIDE), University of Duisburg-Essen, Lotharstraße 1, 47057 Duisburg, Germany*

²*Faculty of Chemistry, University of Duisburg-Essen, Universitätsstraße 5, 45711 Essen, Germany*

³*Institute for Solid State Physics, The University of Tokyo, Kashiwa, Chiba 277-8581, Japan*



(Received 9 December 2022; accepted 1 February 2023; published 13 February 2023)

The transport of optically excited, hot electrons in heterostructures is analyzed by femtosecond, time-resolved two-photon photoelectron emission spectroscopy (2PPE) for epitaxial Au/Fe/MgO(001). We compare the temporal evolution of the 2PPE intensity upon optically pumping Fe or Au, while the probing occurs on the Au surface. In the case of Fe-side pumping, assuming independent relaxation in the Fe and Au layers, we determine the hot electron relaxation times in these individual layers by an analysis of the Au layer thickness dependence of the observed, effective electron lifetimes in the heterostructure. We show in addition that such a systematic analysis fails for the case of Au-side pumping due to the spatially distributed optical excitation density, which varies with the Au layer thickness. This paper extends a previous study [Beyazit *et al.*, *Phys. Rev. Lett.* **125**, 076803 (2020)] with data leading to reduced error bars in the determined lifetimes and by a nonlinear term in the Au thickness-dependent data analysis which contributes to similar Fe and Au film thicknesses.

DOI: [10.1103/PhysRevB.107.085412](https://doi.org/10.1103/PhysRevB.107.085412)

I. INTRODUCTION

Excited electrons in Bloch bands of condensed matter scatter on femtosecond to picosecond timescales due to the strong interaction with bosons and other electrons by e-boson and e-e scattering, respectively [1–4]. Due to the filled valence band in semiconductors, e-phonon coupling dominates the relaxation dynamics in the conduction bands of these materials. In metals, the half-filled bands provide a large phase space for e-e scattering. In addition to the scattering rates as a function of electron energy E and momentum \mathbf{k} , the propagation of such excitations in real space is important to consider from a fundamental point of view as well as in device applications. Finally, gradients in real space induce currents of free charges [1,5] which will heat up the crystal lattice and the device structure by e-ph coupling.

While the decay rates of electronic excitations in metals are by now rather well understood [3,4], the nature of currents on femtosecond and picosecond timescales are a topic of current research, and fundamental questions are of interest. In a seminal study using femtosecond laser pulses in a pump-probe experiment on freestanding Au films, Brorson *et al.* [1] concluded on the ballistic nature of electron currents. On the other hand, it was shown more recently that the analysis of propagation velocities calculated by dividing the film thickness by the propagation time is not accounting for the actual electronic propagation pathway [6–8], and individual e-e scattering processes occur although the determined velocities along the normal direction of the film are close to the Fermi velocity [7].

Such transport phenomena can have considerable influence on the quantitative analysis of hot electron lifetimes [9,10] and transient electron distribution functions [11] centered at the Fermi energy if discarded in surface sensitive methods like photoelectron emission spectroscopy.

Ultrafast electron currents in metals can carry a spin polarization [12], and the resulting spin currents and their interaction with ferromagnetic layers in heterostructures have provided opportunities to control magnetic excitations mediated by spin-pumping, spin-accumulation, and spin-transfer torque [13–20]. These experimental studies rely on magneto-optical or terahertz probes which do not directly access the transient electron distributions. To complement those studies, it is therefore desired to provide energy- and time-resolved information on the propagating electrons.

In the context of spatiotemporal transport effects, it is useful to distinguish the decay dynamics of (i) individual electronic quasiparticles and (ii) hot electron distributions. In the first regime, the decay times measured in time-resolved experiments like two-photon photoelectron emission spectroscopy (2PPE) represent the interaction with further microscopic excitations in response to e-e, e-magnon, and e-ph scattering which is represented by the imaginary part of the self-energy [3,21]. Since no temperature is defined for a single particle, this regime describes by definition a nonthermal limit. In the second regime, the distribution of many electrons is analyzed, and single-particle properties are lost within the distribution. This regime provides insight into the time-dependent energy content of the excited electronic system as a whole and how it interacts with the magnetization or spin polarization [12]. Within simplifying assumptions, it is described, in principle, by the two-temperature model and its derivatives [5,22,23].

*uwe.bovensiepen@uni-due.de

The effect of electron transport in time-resolved photoelectron spectroscopy in the first regime has been analyzed in Beyazit *et al.* [7]. A more recent publication by Kühne *et al.* [24] addresses the second regime and discusses transport effects within the two-temperature model, which allowed them to distinguish diffusive and superdiffusive electron transport. The specific time- and energy-dependent electron dynamics that extends Ref. [7] will provide input to works that so far assumed thermalized distributions [25] or lack sensitivity to nonthermal electrons [26].

In this paper, we report on time-resolved 2PPE results on epitaxial Au/Fe/MgO(001) heterostructures. We directly compare the 2PPE spectra detected on the Au surface in the cases of Fe- and Au-side pumping and analyze the energy-dependent relaxation and propagation times as a function of the Au layer thickness d_{Au} . In the case of Fe-side pumping, the determined relaxation times depend on the energy above the Fermi level $E - E_{\text{F}}$ and on d_{Au} , which is qualitatively explained by a sum of the decay rates in Fe and Au following Matthiesen's rule. In the case of Au-side pumping, this separation fails which is explained by the difference in the optical excitation profiles for Fe- and Au-side pumping. We complement our previous work, Ref. [7], by recently obtained results that are reported here in combination with an extension of the fitting model.

II. EXPERIMENTAL DETAILS

A. Sample Preparation and Characterization

Epitaxial Au-Fe heterostructures were grown on MgO(001) by molecular beam epitaxy. Fe(001) was prepared on the MgO(001) substrate followed by Au(001). As described in Refs. [14,27,28], the in-plane axes of both layers are rotated by $\pi/4$ with respect to each other to minimize the lattice mismatch between Fe and Au which facilitates pseudomorphic growth with an atomically sharp interface. Our earlier work directly analyzes the structure of the buried Fe-Au interface by scanning transmission electron microscopy. It shows that the interface is atomically sharp [14] and that, in the case of more complex heterostructures, the interdiffusion is limited to a few lattice constants [29]. The MgO(001) substrates of $10 \times 10 \text{ mm}^2$ were cleaned in ultrasonic baths of ethanol, isopropanol, and acetone. Subsequently, they were put into ultrahigh vacuum and exposed to O_2 at a partial pressure of 2×10^{-3} mbar at a temperature of 540 K to remove carbon contamination. The Fe layer and the first nanometer of Au were evaporated at 460 K. Then the sample was cooled to room temperature, and the remaining Au was evaporated in the following step-wedge structure. We varied d_{Au} systematically from 5 to 70 nm by growing a wedge-shaped Au layer with 17 steps on a 7-nm-thick Fe layer. Each step is 0.4 mm wide and can be accessed specifically by the laser pulses focused to a spot of $140 \pm 30 \mu\text{m}$ diameter full width at half maximum (FWHM) for the visible pump and $90 \pm 30 \mu\text{m}$ FWHM for the ultraviolet probe. The thicknesses of the Au and Fe layers were determined by secondary ion mass spectroscopy (SIMS), and the depths of the craters induced in SIMS were confirmed subsequently by an independent analysis using a

profilometer. The position of the Fe/Au interface could be determined by a decrease of the SIMS signal to 50% of the Au, while the Fe signal increased to 50%. The thickness of the Fe layer was determined in the same way with the signal increase of the Mg and the signal decrease of the Fe. The error in the film thickness determination is $\pm 10\%$ for all films except for $d_{\text{Au}} = 7 \text{ nm}$, where it is $\pm 20\%$.

B. Time-Resolved 2PPE

Femtosecond laser pulses are generated by a commercial regenerative Ti : sapphire amplifier (Coherent RegA 9040) combined with a noncollinear optical parametric amplifier (NOPA, Clark-MXR) operating at a 250-kHz repetition rate tuned to a signal photon energy of $h\nu = 2.1 \text{ eV}$, which we frequency-doubled in a BBO crystal subsequently. We use these pairs of femtosecond pulses at 2.1 and 4.2 eV with pulse durations $< 40 \text{ fs}$ at a time delay Δt as pump and probe pulses, respectively. The probe pulses reach the Au surface at a 45° angle of incidence. Since the transparent MgO(001) substrate allows direct optical excitation of the Fe layer, the pump pulse can be sent to either the Au or the Fe side of the sample by different pathways, also at a 45° angle of incidence. Thereby, pump and probe laser pulses propagate within their foci simultaneously over the sample which avoids a deterioration of time resolution. Typical incident fluences are 50 and $1 \mu\text{J}/\text{cm}^2$ for pump and probe, respectively. The sample was kept in ultrahigh vacuum and at room temperature. Photoelectrons are detected in normal emission direction from the Au surface by a self-built electron time-of-flight spectrometer [30]. The concept of the 2PPE experiment with a direct comparison of Fe- and Au-side pumping of the Au/Fe/MgO(001) heterostructure is illustrated in Fig. 1(a).

Optical absorption of the pump pulses in the heterostructure differs for Fe- and Au-side pumping since the absorption coefficient of 2-eV photons in Fe is considerably larger than in Au. We have calculated the absorption of the pump pulse in Au/Fe by the electric field inside the material in both pump configurations using IMD software [31] and derived the pump power $P(z)$ in the different constituents with z being the interface normal direction; $z = 0$ is set to the Fe-Au interface:

$$P(z) = n(z)I(z) = n(z)|E(z)|^2 = n(z)I_0e^{-\alpha z}, \quad (1)$$

Here, α is the absorption coefficient, $I(z)$ the intensity, $E(z)$ the electric field, and $n(z)$ the refractive index in the respective material. The power in the layer stack is given by the real part of the Poynting vector. Figure 1 depicts the normalized intensity (dashed lines, left axes) for (b) Fe-side and (c) Au-side pumping. The relative absorbed power $P_a(z)$ was obtained by subtracting the transmitted power and normalizing to the absorbed power because we focus on the attenuation of the field by absorption (solid lines, right axes). $P_a(z) = [P(z) - P_T]/(P_I - P_T)$, where P_I and P_T are the incident and transmitted pump power, respectively. We considered the pump photon energy of 2.1 eV, the angle of incidence $\theta = 45^\circ$, the p -polarization of the light, the refractive indices $n_{\text{Au}}(2.1 \text{ eV}) = 0.25$, $n_{\text{Fe}}(2.1 \text{ eV}) = 2.91$, and the extinction coefficients $k_{\text{Au}}(2.1 \text{ eV}) = 3.07$, $k_{\text{Fe}}(2.1 \text{ eV}) = 3.02$ [32] with $\alpha = 4\pi k/\lambda$; λ is the optical wavelength. We find that, in the case of Fe-side pumping, the absorption is dominated by the Fe layer: 96% for

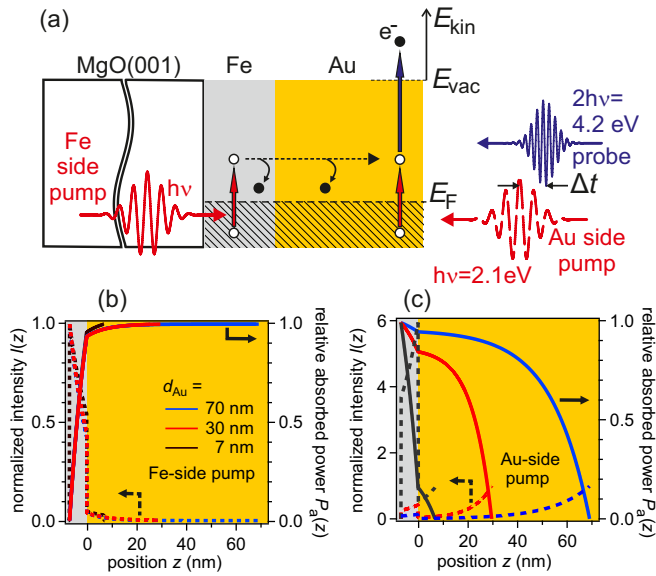


FIG. 1. (a) Experimental geometry of the pump-probe experiment with Fe- and Au-side pumping of Au/Fe/MgO(001) heterostructures by visible femtosecond laser pulses at $h\nu = 2.1$ eV photon energy. Probing occurs by analysis of the two-photon photoelectron emission spectrum at the Au surface induced by $2h\nu = 4.2$ eV. In the case of Fe-side pumping, electrons must propagate to the Au surface before being probed. Spatial distribution of the excitation density by the calculated pump intensity $I(z)$ with respect to the incident light field (dashed lines, left axes) and the relative absorbed pump power $P_a(z)$ (solid lines, right axes) as a function of Au layer thickness for (b) Fe-side and (c) Au-side pumping. Please see the text for details. The thickness of the Fe layer is 7 nm (gray area). Note that the nominal maximum intensity in (c) is higher at the interface than in (b) because of the change in optical constants for a change in layer sequence.

$d_{Au} = 7$ nm and 94% for $d_{Au} = 70$ nm. In the case of Au-side pumping, the situation is diverse. A pronounced variation in the relative intensity occurs at the Fe-Au interface, where the refractive index changes and the light field is attenuated in Au before it reaches Fe. Note, that for $d_{Au} = 7$ nm, the dominant absorption occurs in Fe though it reaches Au first. For thicker Au layers, the pump absorption is distributed over the Au layer.

III. EXPERIMENTAL RESULTS AND DATA ANALYSIS

The time-resolved 2PPE intensity was measured as a function of d_{Au} on the step-wedged sample, and representative results are shown in Fig. 2 after subtraction of time-independent contributions originating from multiphoton photoemission within a single pump or probe pulse, which is typically 10% of the time-dependent intensity. Characteristic changes with increasing d_{Au} for Fe-side pumping are a reduced intensity at $E - E_F = 1.7$ eV and a shift of the intensity maximum at lower energy near $E - E_F = 0.6$ eV to later Δt . For Au-side pumping, the maximum intensity is found at a peak close to the top end of the spectrum at 1.7 eV independent of d_{Au} . This peak is assigned to image potential states in front of the Au surface [33]. Since these states are

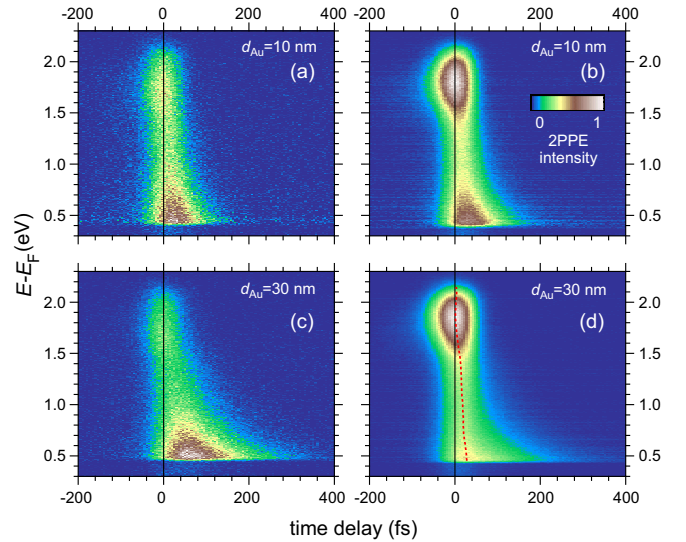


FIG. 2. Representative two-photon photoelectron emission spectroscopy (2PPE) intensity as a function of time delay and energy above the Fermi level in a false color representation for $d_{Fe} = 7$ nm and $d_{Au} = 10$ and 30 nm, as indicated; (a) and (c) Fe-side pumping, (b) and (d) Au-side pumping. The red, dashed line in (d) indicates the 2PPE intensity maxima for different energies with time delay.

bound to the vacuum energy at the Au surface and not the Fermi energy of the layer stack, they will not be discussed further here.

For all datasets, an increase in intensity toward lower $E - E_F$ and later Δt is recognized, which can be weaker or stronger depending on d_{Au} or the pumping geometry. This effect has two origins. (i) The hot electron lifetime increases according to Fermi-liquid theory $\propto (E - E_F)^{-2}$ [3,4]. (ii) At electron energies $E - E_F$ below half of the pump photon energy, secondary electrons will contribute to the 2PPE intensity [10]. In this paper, we focus on the analysis of the hot electron lifetimes, i.e., the inverse rate of the primary inelastic scattering event, for which 2PPE is the appropriate method. Thereby, we analyze nonthermal transport since electron thermalization has not yet taken place. The contribution of secondary electrons, effects toward electron thermalization upon Fe- and Au-side pumping, and thermal electron transport were reported recently in Ref. [24] based on time-resolved linear photoelectron emission spectroscopy.

For both pump geometries, $\Delta t = 0$ was determined for consistency by the 2PPE intensity maximum at the highest energy at the top end of the spectrum. We note that there is a certain ambiguity in this choice of time zero. For Fe-side pumping, a certain propagation time of the excited electron through the layer stack before the electron is detected at the Au surface occurs. For Au-side pumping, the spectrally broad image potential state feature could extend up to the top end of the spectrum. As a consequence, the chosen $\Delta t = 0$ would be shifted to negative time delays since the finite decay time of the image potential states convoluted with the pulse duration results in an effective shift of the intensity maximum since the trailing part of the probe laser pulse contributes to the signal. To estimate this potential inaccuracy in the determination of $\Delta t = 0$, we indicate in Fig. 2(d) the intensity maxima

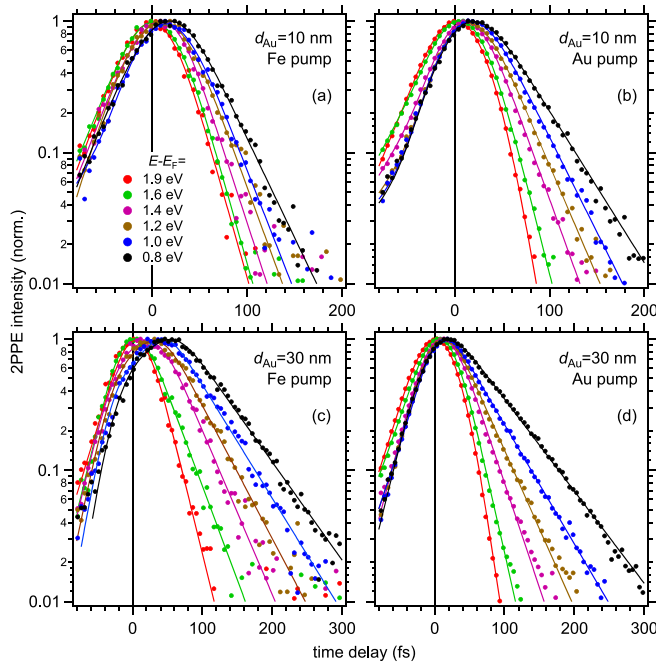


FIG. 3. Normalized two-photon photoelectron emission spectroscopy (2PPE) intensity as a function of time delay at different energies $E - E_F$ for $d_{\text{Fe}} = 7$ nm and d_{Au} and pumping as indicated in (a)–(d). The dots are experimental data, the lines represent least-square fits using an exponential relaxation convoluted with a Gaussian, see text for details. Note that different intervals in time delay are depicted in (a), (b) and (c), (d).

as a function of Δt for all energies by a dashed red line. At $E - E_F = 1.5$ – 1.0 eV, the maximum is shifted to $+15$ fs without a clear decay. We consider in the following that the actual time zero is uncertain within this interval of 0–15 fs.

Similar measurements were taken for 13 different d_{Au} 's in the case of Fe-side pumping and 7 different d_{Au} 's in the case of Au-side pumping. We analyzed the time-dependent 2PPE intensities at constant energy $E - E_F$ for all these measurements after normalization to the time-dependent peak maximum. Typical examples of such datasets are shown in Fig. 3 for the data of Fig. 2. A comparison of these traces for d_{Au} in panels (c) and (d) for both pumping geometries highlights that the time delays of the intensity maxima are shifted for Fe-side pumping toward later Δt much more than for Au-side pumping. This effect is attributed to propagation of the electronic excitation through the Au layer and quantified by a time offset t_0 , see Ref. [7] for a discussion of the results on t_0 . These traces are fitted for both pumping geometries with two exponential decays, one toward negative Δt to account for the contribution excited by 4.2 eV photons and one for the decay toward positive Δt excited by 2.1 eV photons shifted by t_0 . All is convoluted with a Gaussian of ~ 50 fs width to account for the cross-correlation of the laser pulses. The resulting fits are included in Fig. 3 by solid lines.

For a discussion of the determined lifetimes, it is important to consider that the excited electron can relax in the Fe or in the Au layer of the heterostructure. If it does not relax in Fe, we assume in the following analysis that the electron is injected elastically into the Au layer where it relaxes

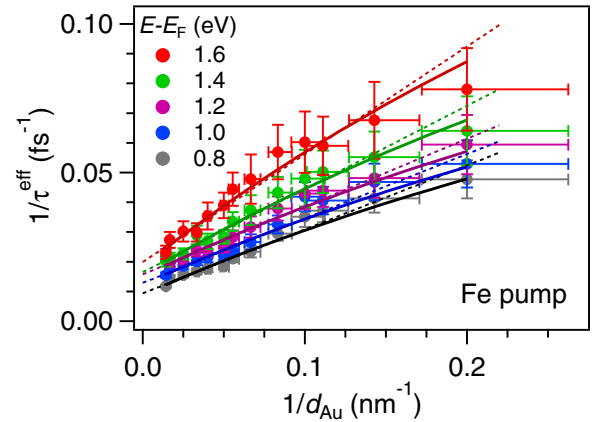


FIG. 4. The relaxation rates determined from the inverse hot electron lifetimes in the case of Fe-side pumping are plotted as filled circles for energies above E_F as a function of the inverse Au layer thickness. The solid (dotted) lines depict nonlinear (linear) functions fitted to the relaxation rates at the energy represented by the indicated color code. See the text for details.

subsequently. This is rationalized with the single-crystalline interface structure [14] and by the fact that no interface decay contribution is required to describe the data, as discussed below. For the Fe-side pumping and Au-side probing geometry, the detected electron has to propagate through the layer stack, and the probability for an electron to decay will increase in both layers with their respective thicknesses. In the limit of a sufficiently thin Fe layer, which is grown on the insulating MgO(001), transport effects can be neglected in Fe. Supposing that the Au layer grown on top of Fe is sufficiently thin that its contribution to the decay probability can be neglected, this experimental geometry would be expected to measure the relaxation dynamics in Fe. Vice versa, if the Fe layer is very thin and the Au layer is sufficiently thick, the relaxation dynamics in Au would be measured. As a function of d_{Au} , we can therefore expect to detect a combination of relaxation in the Fe and Au constituents as suggested by Mathiessens's rule. The data presented in Fig. 3 clearly show a faster relaxation for $d_{\text{Au}} = 10$ nm than $d_{\text{Au}} = 30$ nm for both Fe- and Au-side pumping. To test this hypothesis, we analyze the inverse relaxation times as a function of d_{Au} as a linear function of $1/d_{\text{Au}}$ to account for the variation of the decay contribution in Au by

$$\frac{1}{\tau^{\text{eff}}(d_{\text{Au}})} = A + \frac{B}{d_{\text{Au}}}. \quad (2)$$

In this empirical limit, $1/A = \tau_{\text{Au}}$ and $1/B = \tau_{\text{Fe}}^0/d_{\text{Au}}^0$, where d_{Au}^0 normalizes d_{Au} and is chosen as 1 nm. Figure 4 shows the respective analysis. The linear functions of Eq. (2) are included as dotted lines which fit the experimental data reasonably well within the error bars. At large $1/d_{\text{Au}}$, we observe systematic deviations of the linear fit from the experimental results. The fit tends to overestimate the measured relaxation rates. In the following, we derive a suitable nonlinear correction. The corresponding fits are plotted as solid lines in Fig. 4.

Under the approximation that the electronic velocity in Fe and Au is similar and that scattering at the Fe-Au interface

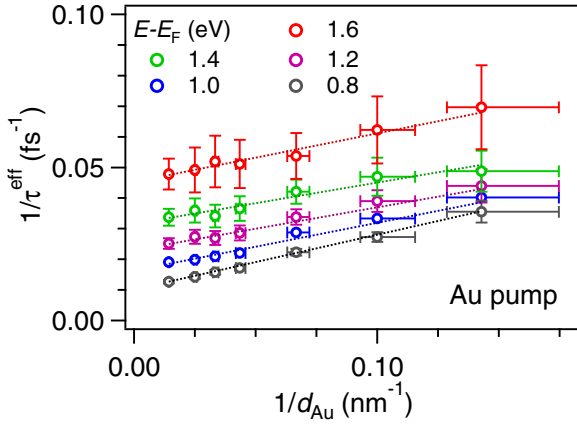


FIG. 5. The relaxation rates determined from the inverse hot electron lifetimes in the case of Au-side pumping, see text for details, are plotted as open circles for energies above E_F as a function of the inverse Au layer thickness. The dotted lines are linear fits to the relaxation rates at the energy represented by the indicated color code.

can be discarded, the scattering probability in the layer stack $1/\tau^{\text{eff}}$ is determined by d_{Au} and d_{Fe} [7] following

$$\frac{d_{\text{Au}} + d_{\text{Fe}}}{\tau^{\text{eff}}} = \frac{d_{\text{Au}}}{\tau_{\text{Au}}} + \frac{d_{\text{Fe}}}{\tau_{\text{Fe}}}. \quad (3)$$

Since d_{Au} was varied and d_{Fe} was kept constant at 7 nm,

$$\frac{1}{\tau^{\text{eff}}(d_{\text{Au}})} = \frac{d_{\text{Au}}}{d_{\text{Fe}}^{\text{eff}} + d_{\text{Au}}} \frac{1}{\tau_{\text{Au}}} + \frac{d_{\text{Fe}}^{\text{eff}}}{d_{\text{Fe}}^{\text{eff}} + d_{\text{Au}}} \frac{1}{\tau_{\text{Fe}}}. \quad (4)$$

As discussed below in Sec. IV, we introduce $d_{\text{Fe}}^{\text{eff}}$ to account for the optical inhomogeneous pumping of Fe and for different electron velocities in Fe and Au. For $d_{\text{Au}} \gg d_{\text{Fe}}^{\text{eff}}$, the factor of the first term becomes one and the one of the second term tends to reduce to $1/d_{\text{Au}}$ as in Eq. (2). For $d_{\text{Au}} \approx d_{\text{Fe}}^{\text{eff}}$, the fitting by Eq. (4) overcomes the previous deviation between experimental data and improves the fitting using Eq. (2) for thin Au films, see Fig. 4.

This analysis potentially also holds for the experiments which employ Au-side pumping. To test this hypothesis, we plot $1/\tau^{\text{eff}}$ obtained for Au-side pumping as a function of $1/d_{\text{Au}}$ and fit the data by Eq. (2). The results are shown in Fig. 5. In this case, the linear fitting describes the data very well, but the quantitative behavior of the results for A and B as a function of $E - E_F$ differs from the results obtained for Fe-side pumping, c.f. Fig. 4. For Au-side pumping, the slope B increases with decreasing energy, while the opposite trend is found for Fe-side pumping. In addition, the offset A is about two times larger than for Fe-side pumping.

The results for τ_{Au} and τ_{Fe} obtained for the linear and nonlinear analysis in the Fe-side and for the linear analysis in the Au-side pumping geometry are compiled as a function of energy in Fig. 6. We also include literature data for hot electron lifetimes in bulk Au and Fe taken from Bauer *et al.* [4] for comparison. The findings for τ_{Au} and τ_{Fe} in the case of Fe-side pumping are in very good agreement with the literature data, which holds for both fitting models. We conclude that, for Fe-side pumping, a separation of the relaxation dynamics in the Fe and Au constituents is successful. We

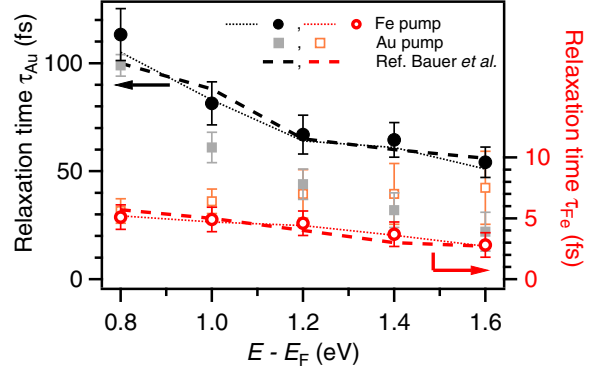


FIG. 6. Filled and open circles are the best fit results of τ_{Fe} and τ_{Au} by the Au thickness-dependent analysis of the hot electron lifetimes in the case of Fe-side pumping using the nonlinear fitting analysis. The results for the linear fitting are depicted by thin dotted lines. Open and filled squares are the corresponding results for Au-side pumping. Dashed lines represent literature data for hot electron lifetimes for bulk Fe and Au [4]. Black and gray data for τ_{Au} are referred to the left axis, red and orange data for τ_{Fe} to the right axis.

note that the nonlinear fitting required to assume a value of $d_{\text{Fe}}^{\text{eff}} = 1.3 \pm 0.2$ nm which is much smaller than the actual Fe film thickness of $d_{\text{Fe}} = 7$ nm to obtain this agreement. This result is discussed in the Sec. IV below. In the case of Au-side pumping, the deviation of the experimental data points and the literature data is significant for $E - E_F > 0.8$ eV. In this experimental geometry, the separation of the dynamics in the two constituents fails.

IV. DISCUSSION

Hot electron transport phenomena have been widely identified and discussed in the literature of pump-probe experiments in which pump and probe pulses impinge at the sample surface from the identical side, see, e.g., Refs. [5,9–11,13,19,34–36]. We showed in this paper that profound differences occur in the quantitative analysis for two experimental configurations in which pump and probe pulses arrive at the same or opposite sides of the sample surface. These differences are not primarily related to the analysis of the transport phenomenon itself but have effects on the determined hot electron lifetimes. This aspect might be particularly relevant in heterostructure samples where electrons can be transferred among different constituents. We explain these differences between Fe- and Au-side pumping by the different pump absorption profiles in the heterostructure. As shown in Figs. 1(b) and 1(c), the absorption profile is very different for the two pumping geometries. For the Fe-side pumping, the hot electrons are primarily excited in Fe and propagate a well-defined distance to the Au surface, where the photoelectrons are detected. In the Au-side pumping situation, the electrons are excited in Fe and Au with different spatial profiles depending on d_{Au} . Since the electronic transport processes are determined by gradients in excitation density and electronic temperature [5], the velocity distributions and the corresponding transient electron densities will differ for the two pumping geometries. Therefore, it is not only the opposite direction of the pump-induced transport that distinguishes Au- and Fe-side pumping. The quantitative difference in the absolute values of

the spatial gradients of the excitation density leads to spatial redistribution of transient electron density which was already recognized to result in misleading lifetime analysis [9,10]. The wider spatial distribution of the excited electrons that cover Fe and Au in the case of Au-side pumping inhibits the separation of the dynamics in this case. So far, the back-side pump and front-side probe configuration proved to be a very suitable approach to analyze electron scattering and transport for the material system under study.

The nonlinear fitting approach in the analysis of the hot electron lifetimes for Fe-side pumping resulted in the finding that $d_{\text{Fe}}^{\text{eff}} = 1.3$ nm is much thinner than the actual $d_{\text{Fe}} = 7$ nm. Here, we discuss two aspects in this context to rationalize this result. (i) Figure 1(b) depicts the variation of absorbed pump intensity which changes two times across the Fe layer. A corresponding spatial distribution of excited electrons is injected from Fe to Au. Consequently, the average distance an electron has to travel before it reaches the Fe-Au interface is 3–4 nm. (ii) In deriving Eq. (4), we assumed that the electronic velocities in Fe and Au are similar. In fact, they differ at the relevant energies considerably according to GW calculations [37]. For most electrons in Fe, the velocity is 0.6 of the one in Au at $E - E_{\text{F}} = 1.5$ eV. To compensate for this difference in velocity, a correspondingly thinner Fe sheet might be considered as effective since, in the time interval before scattering occurs, an electron can cover a shorter pathway at a lower velocity. We discard here minority electrons in Fe since the injection probability across the Fe-Au interface favors injection of majority electrons [29]. Both these effects reduce the effective Fe film thickness in hot electron injection to Au, and the result obtained for $d_{\text{Fe}}^{\text{eff}}$ is very plausible.

The model considers quasiparticle lifetimes of individual excited electrons. It is accounting for nonthermal electrons because electron thermalization is the result of the decay of these electrons and their interaction with other electrons. Since these lifetimes are dominated by the e-e scattering probability, the secondary electrons generated in this scattering form a thermalized distribution in the vicinity of the Fermi energy. Considering the incident pump fluence of $50 \mu\text{J}/\text{cm}^2$, a corresponding hot electron temperature increase is on the order of 100 K, see Kühne *et al.* [24] for further discussion of this aspect. In the present 2PPE experiment, electrons at the Fermi energy are not detected. As such, we do not discuss thermal transport here but in Ref. [24]. Therefore, the timescales in this paper are considerably shorter than those reported in Ref. [26] and experiments in similar regimes.

Finally, we discuss the potential impact of our work on other problems. In this paper, we quantify the energy-dependent electron dynamics upon Au- and Fe-side optical excitation, which complements a recently published study [24] which used linear time-resolved photoelectron detection to study the electron distribution near E_{F} . Both these works might serve as input for electron dynamics in the description of optically excited spin currents in metallic heterostructures. A description of these currents by thermal models can be considered as simplified, though they potentially describe the spin currents reasonably well.

An extension of the presented approach to spin-resolved photoelectron spectroscopy appears as promising given the recent development of efficient spin-resolved photoelectron

analysis [38]. A 2PPE experiment will very likely be more suitable than detection in time-resolved linear photoelectron emission [26] since it provides higher count rates of photoelectrons that carry time-resolved information.

Previous interest in time-resolved spectroscopic information in layered perovskite systems upon optical excitation at the opposite sample side [39] suggests an extension of the approach reported in this paper to further material systems. Our study can be considered to address a rather favorable problem since, due to the excellent interface structure, the scattering centers at the interface were sufficiently small in density that they did not have to be considered explicitly. For other material systems, this might be different, particularly for structures that promise technological relevance like, e.g., the mentioned perovskite systems. In such a situation, interface scattering could be analyzed by variation of the two film thicknesses separately [7]. Another potential direction of experiments that builds on our demonstration is the use of Au/Fe/MgO(001) as electrodes for hot electrons injected into solid layers prepared on top of Au. This is a promising future research opportunity for solid layered materials. It is also interesting to consider this approach in combination with liquid electrolytes. In this case, the detection of photoelectrons could be very challenging, but the detection by a surface sensitive nonlinear optical technique might be viable [14].

V. CONCLUSIONS

The ultrafast transport of optically excited hot electrons in epitaxial Au/Fe/MgO(001) heterostructures is studied by systematically varying the Au layer thickness. The results presented here extend our earlier study on this heterostructure and enabled a determination of hot electron lifetimes for the Fe and Au constituents separately with reduced error. This analysis implies a nonlinear dependence of the effective relaxation rate on the Au layer thickness. It was successful in attributing a systematic deviation at smaller Au layer thickness, in the range of the Fe layer thickness, from its dependence on thicker Au layers for the Fe-side pumping configuration. The success of the analysis in the case of Fe-side pumping is attributed to its ability to excite carriers in a specific part in the heterostructure independently on the propagation pathway before detection. Front- and back-side pumping studies are commonly used for studying transport-induced effects in nanostructures; however, we showed here that the spatial distribution of the excitation density plays a strong role in modifying the measured results. The results presented here will serve as input for electron dynamics in the description of spin currents in metallic heterostructures, their interfaces, and hot electrons injected into other coupled systems which are of technological importance.

ACKNOWLEDGMENTS

Funding by the Deutsche Forschungsgemeinschaft through Project No. 278162697—SFB 1242, through Project No. BO1823/12—FOR 5249 (QUAST), and under Germany's Excellence Strategy—EXC 2033—390677874—RESOLV is gratefully acknowledged. We are also grateful for fruitful discussions with J. Beckord.

- [1] S. D. Brorson, J. G. Fujimoto, and E. P. Ippen, *Phys. Rev. Lett.* **59**, 1962 (1987).
- [2] J. Shah, *Ultrafast Spectroscopy of Semiconductors and Semiconductor Nanostructures*, 2nd ed. (Springer, Berlin, Heidelberg, 1999).
- [3] E. V. Chulkov, A. G. Borisov, J. P. Gauyacq, D. Sánchez-Portal, V. M. Silkin, V. P. Zhukov, and P. M. Echenique, *Chem. Rev.* **106**, 4160 (2006).
- [4] M. Bauer, A. Marienfeld, and M. Aeschlimann, *Prog. Surf. Sci.* **90**, 319 (2015).
- [5] J. Hohlfeld, S. S. Wellershoff, J. Güdde, U. Conrad, V. Jähnke, and E. Matthias, *Chem. Phys.* **251**, 237 (2000).
- [6] X. Liu, R. Stock, and W. Rudolph, *Phys. Rev. B* **72**, 195431 (2005).
- [7] Y. Beyazit, J. Beckord, P. Zhou, J. P. Meyburg, F. Kühne, D. Diesing, M. Ligges, and U. Bovensiepen, *Phys. Rev. Lett.* **125**, 076803 (2020).
- [8] A. Melnikov, L. Brandt, N. Liebing, M. Ribow, I. Mertig, and G. Woltersdorf, *Phys. Rev. B* **106**, 104417 (2022).
- [9] M. Aeschlimann, M. Bauer, S. Pawlik, R. Knorren, G. Bouzerar, and K. H. Bennemann, *Appl. Phys. A: Mater. Sci. Process.* **71**, 485 (2000).
- [10] M. Lisowski, P. A. Loukakos, U. Bovensiepen, and M. Wolf, *Appl. Phys. A* **79**, 739 (2004).
- [11] M. Lisowski, P. A. Loukakos, U. Bovensiepen, J. Stähler, C. Gahl, and M. Wolf, *Appl. Phys. A: Mater. Sci. Process.* **78**, 165 (2004).
- [12] M. Battiato, K. Carva, and P. M. Oppeneer, *Phys. Rev. Lett.* **105**, 027203 (2010).
- [13] G. Malinowski, F. D. Longa, J. H. H. Rietjens, P. V. Paluskar, R. Huijink, H. J. M. Swagen, and B. Koopmans, *Nat. Phys.* **4**, 855 (2008).
- [14] A. Melnikov, I. Razdolski, T. O. Wehling, E. T. Papaioannou, V. Roddatis, P. Fumagalli, O. Aktsipetrov, A. I. Lichtenstein, and U. Bovensiepen, *Phys. Rev. Lett.* **107**, 076601 (2011).
- [15] N. Bergeard, M. Hehn, S. Mangin, G. Lengaigne, F. Montaigne, M. L. M. Laliou, B. Koopmans, and G. Malinowski, *Phys. Rev. Lett.* **117**, 147203 (2016).
- [16] I. Razdolski, A. Alekhin, N. Ilin, J. P. Meyburg, V. Roddatis, D. Diesing, U. Bovensiepen, and A. Melnikov, *Nat. Commun.* **8**, 15007 (2017).
- [17] F. Hellman, A. Hoffmann, Y. Tserkovnyak, G. S. D. Beach, E. E. Fullerton, C. Leighton, A. H. MacDonald, D. C. Ralph, D. A. Arena, H. A. Dürr *et al.*, *Rev. Mod. Phys.* **89**, 025006 (2017).
- [18] D. M. Nenno, B. Rethfeld, and H. C. Schneider, *Phys. Rev. B* **98**, 224416 (2018).
- [19] J. Chen, U. Bovensiepen, A. Eschenlohr, T. Müller, P. Elliott, E. K. U. Gross, J. K. Dewhurst, and S. Sharma, *Phys. Rev. Lett.* **122**, 067202 (2019).
- [20] V. H. Ortiz, S. Coh, and R. B. Wilson, *Phys. Rev. B* **106**, 014410 (2022).
- [21] M. Weinelt, *J. Phys.: Condens. Matter* **14**, R1099 (2002).
- [22] U. Bovensiepen, *J. Phys.: Condens. Matter* **19**, 083201 (2007).
- [23] B. Koopmans, G. Malinowski, F. D. Longa, D. Steiauf, M. Fähnle, T. Roth, M. Cinchetti, and M. Aeschlimann, *Nat. Mater.* **9**, 259 (2010).
- [24] F. Kühne, Y. Beyazit, B. Sothmann, J. Jayabalan, D. Diesing, P. Zhou, and U. Bovensiepen, *Phys. Rev. Res.* **4**, 033239 (2022).
- [25] M. Beens, R. A. Duine, and B. Koopmans, *Phys. Rev. B* **105**, 144420 (2022).
- [26] K. Bühlmann, G. Saerens, A. Vaterlaus, and Y. Acremann, *Sci. Rep.* **10**, 12632 (2020).
- [27] Th. Möhge, A. Stierle, N. Metoki, H. Zabel, and U. Pietsch, *Appl. Phys. A* **59**, 659 (1994).
- [28] M. Mattern, A. von Reppert, S. P. Zeuschner, J.-E. Pudell, F. Kühne, D. Diesing, M. Herzog, and M. Bargheer, *Appl. Phys. Lett.* **120**, 092401 (2022).
- [29] A. Alekhin, I. Razdolski, N. Ilin, J. P. Meyburg, D. Diesing, V. Roddatis, I. Rungger, M. Stamenova, S. Sanvito, U. Bovensiepen *et al.*, *Phys. Rev. Lett.* **119**, 017202 (2017).
- [30] P. S. Kirchmann, L. Rettig, D. Nandi, U. Lipowski, M. Wolf, and U. Bovensiepen, *Appl. Phys. A* **91**, 211 (2008).
- [31] D. L. Windt, *Comput. Phys.* **12**, 360 (1998).
- [32] E. D. Palik, *Handbook of Optical Constants of Solids*, 1st ed., Vol. III (Academic Press, San Diego, 1997).
- [33] This peak is assigned to image potential states in front of the Au surface [40] in response to the sequence of pumping with 4.2 eV and probing with 2.1 eV, opposite compared with the sequence discussed in this paper. This sequence leads to population decay with nominally negative time delays. The energy of the peak corresponds therefore to $E - E_F = 3.8$ eV, which is obtained by adding the photon energy to the energy indicated in Fig. 2. The observed spectral linewidth indicates inhomogeneous broadening due to the remaining surface inhomogeneity. Within the temporal overlap of the ultrashort pump and probe pulses, the time-dependent, nonlinear polarization and the population buildup, which is mediated by dephasing of the polarization, both lead to 2PPE intensity but with different intermediate state energy [21,41]. These two contributions overlap since their final state energy detected in the electron spectrometer is identical.
- [34] A. J. Schellekens, K. C. Kuiper, R. de Wit, and B. Koopmans, *Nat. Commun.* **5**, 4333 (2014).
- [35] J. Wiczorek, A. Eschenlohr, B. Weidtmann, M. Rösner, N. Bergeard, A. Tarasevitch, T. O. Wehling, and U. Bovensiepen, *Phys. Rev. B* **92**, 174410 (2015).
- [36] J. Chen, J. Wiczorek, A. Eschenlohr, S. Xiao, A. Tarasevitch, and U. Bovensiepen, *Appl. Phys. Lett.* **110**, 092407 (2017).
- [37] V. P. Zhukov, E. V. Chulkov, and P. M. Echenique, *Phys. Rev. B* **73**, 125105 (2006).
- [38] G. Schönhense, K. Medjanik, and H.-J. Elmers, *J. Electron Spectrosc. Relat. Phenom.* **200**, 94 (2015).
- [39] J. Sung, C. Schnedermann, L. Ni, A. Sadhanala, R. Y. S. Chen, C. Cho, L. Priest, J. M. Lim, H.-K. Kimand, B. Monserrat *et al.*, *Nat. Phys.* **16**, 171 (2020).
- [40] P. M. Echenique, R. Berndt, E. Chulkov, T. Fauster, A. Goldmann, and U. Höfer, *Surf. Sci. Rep.* **52**, 219 (2004).
- [41] H. Petek and S. Ogawa, *Prog. Surf. Sci.* **56**, 239 (1997).